

Complex electronic topography and magnetotransport in an in-plane ferromagnetic kagome metal

Anup Pradhan Sakhya,¹ Richa Pokharel Madhogaria,² Barun Ghosh,^{3,4} Nabil Atlam,^{3,4} Milo Sprague,¹ Mazharul Islam Mondal,¹ Himanshu Sheokand,¹ Arun K. Kumay,¹ Shirin Mozaffari,² Rui Xue,² Yong P. Chen,⁵ David G. Mandrus,^{2,6,7} Arun Bansil,^{3,4} and Madhab Neupane^{1,*}

¹Department of Physics, University of Central Florida, Orlando, Florida 32816, USA

²Department of Materials Science and Engineering, The University of Tennessee, Knoxville, Tennessee 37996, USA

³Department of Physics, Northeastern University, Boston, Massachusetts 02115, USA

⁴Quantum Materials and Sensing Institute, Northeastern University, Burlington, Massachusetts 01803, USA

⁵Department of Physics and Astronomy and Purdue Quantum Science and Engineering Institute, Purdue University, West Lafayette, Indiana 47907, USA

⁶Department of Physics and Astronomy, University of Tennessee Knoxville, Knoxville, Tennessee 37996, USA

⁷Materials Science and Technology Division, Oak Ridge National Laboratory, Oak Ridge, Tennessee 37831, USA

(Dated: May 16, 2025)

The intricate interplay between flat bands, Dirac cones, and magnetism in kagome materials has recently attracted significant attention from materials scientists, particularly in compounds belonging to the RMn_6Sn_6 family ($R = \text{Sc}, \text{Y}$, rare-earths), due to their inherent magnetic frustration. Here, we present a detailed investigation of the ferromagnetic (FM) kagome magnet $\text{ScMn}_6(\text{Sn}_{0.78}\text{Ga}_{0.22})_6$ using angle-resolved photoemission spectroscopy (ARPES), magnetotransport measurements, and density functional theory (DFT) calculations. Our findings reveal a paramagnetic-to-FM transition at 375 K, with the in-plane direction serving as the easy magnetization axis. Notably, ARPES measurements reveal a Dirac cone near the Fermi energy, while the Hall resistivity exhibits a substantial contribution from the anomalous Hall effect. Additionally, we observe a flat band spanning a substantial portion of the Brillouin zone, arising from the destructive interference of wave functions in the Mn kagome lattice. Theoretical calculations reveal that the gap in the Dirac cone can be modulated by altering the orientation of the magnetic moment. An out-of-plane orientation produces a gap of approximately ~ 15 meV, while an in-plane alignment leads to a gapless state, as corroborated by ARPES measurements. This comprehensive analysis provides valuable insights into the electronic structure of magnetic kagome materials and paves the way for exploring novel topological phases in this material class.

Kagome materials have generated considerable excitement in recent years due to their manifestation of various novel topological and correlated electronic phenomena [1–17]. The kagome lattice consists of a two-dimensional honeycomb network characterized by alternating, corner-sharing triangles that form a hexagonal structure. Analysis using a simple tight-binding model has revealed a band structure featuring Dirac cones, Van Hove singularities, and flat bands, all emerging from this unique lattice geometry [9]. These flat bands offer a versatile platform for exploring exotic correlated electron phenomena, where interaction energy dominates over kinetic energy [9]. Incorporating spin-orbit coupling (SOC) and magnetism can open a gap in the Dirac band at the corners of the Brillouin zone (BZ), leading to the emergence of intrinsic Chern quantum phases. This, in turn, results in a significant intrinsic anomalous Hall effect (AHE) arising from the Berry curvature of Dirac cones [3, 6, 18–20]. Recent discoveries have uncovered several kagome magnets exhibiting exotic topological states and other intriguing phenomena. Notable examples include massive Dirac fermions in Fe_3Sn_2 [3], a giant intrinsic anomalous Hall effect in the antiferromagnets Mn_3Sn and Mn_3Ge , and the identification of the magnetic Weyl semimetal $\text{Co}_3\text{Sn}_2\text{S}_2$ [21–23].

The RMn_6Sn_6 family (where R represents rare-earth elements) has recently become a focal point of research [6, 10, 24–32]. In LiMn_6Sn_6 , significant contributions to the anomalous

Hall effect have been attributed to band crossings near the Fermi energy [33]. Additionally, Chern-gapped massive Dirac fermions have been identified within the RMn_6Sn_6 family, which features a FM Mn kagome lattice [24]. Observations of Landau quantization and the appearance of a Landau fan diagram in TbMn_6Sn_6 further indicate the existence of massive Dirac fermions at the K point [6]. Several members of the RMn_6Sn_6 family ($R = \text{Gd-Dy}, \text{Y}$) have been reported to host Dirac fermions and flat bands arising from the Mn magnetic kagome lattice, leading to a significant Berry curvature in momentum space [10, 25, 26].

Additionally, intrinsic anomalous Hall conductivity has been observed in ferrimagnetic RMn_6Sn_6 ($R = \text{Gd-Ho}$) and helical antiferromagnetic (AFM) YMn_6Sn_6 materials [24, 27, 28, 34, 35]. Furthermore, a topological Hall effect has been observed in YMn_6Sn_6 , ErMn_6Sn_6 , and HoMn_6Sn_6 , attributed to the complex magnetic structures in these materials [30, 31, 36, 37]. As a result, significant attention is being directed towards experimental investigations of various members of the RMn_6Sn_6 family. The magnetic phases in these materials play a central role in their intriguing properties, necessitating a comprehensive approach to understanding the intricate magnetic interactions and their manifestation in the topological surface states.

This study focuses on investigating the influence of spin-orbit interaction and FM ordering on Ga-doped ScMn_6Sn_6 . The undoped ScMn_6Sn_6 compound exhibits semimetallic behavior and has a hexagonal crystal structure, isostructural to HfGe_6Sn_6 , within the symmetry group $P6/mmm$ (No. 191).

* Corresponding author: madhab.neupane@ucf.edu

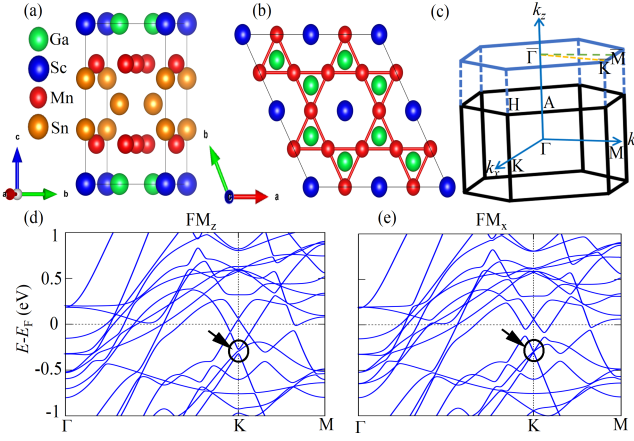


Fig. 1. Theoretical modulation of Dirac gap through magnetization direction tuning. (a) Side view and (b) Top view of the crystal structure of $\text{ScMn}_6(\text{Sn}_{0.78}\text{Ga}_{0.22})_6$. Green, Blue, Red, and Orange colored balls represent Ga, Sc, Mn, and Sn atoms, respectively. (c) Bulk BZ and the projection on the (001) surface BZ with marked high-symmetry points. (d) Bulk band structure along the Γ -K-M high symmetry directions calculated with the spin-quantization direction along the [001] and (e) [100] directions, respectively. Spin-orbit coupling is considered in the calculations.

Its lattice parameters are characterized by $a = b = 5.465 \text{ \AA}$ and $c = 8.96 \text{ \AA}$. This layered material consists of alternating Mn and Sn layers [38, 39]. The Mn layers form an electronically isolated two-dimensional kagome lattice, while one of the Sn layer adopts a hexagonal crystal structure. Pristine ScMn_6Sn_6 is composed of double-layered manganese kagome sheets, separated by alternating Sn and Sc-Sn sublayers. In these kagome sheets, the magnetic spins align ferromagnetically within the plane and are connected helically along the c -axis [40]. Below the Néel temperature (T_N) of 390 K, ScMn_6Sn_6 undergoes AFM ordering, exhibiting multiple magnetic transitions with increasing external magnetic field [41]. This family of compounds displays various magnetic phases, including ferromagnetism, ferrimagnetism, antiferromagnetism, and helical ordering, reflecting the complex competition between magnetic phases. Consequently, the delicate magnetic phases in ScMn_6Sn_6 can be modulated by doping at the Sn sites. Gallium doping stabilizes the FM phase. In this study, ScMn_6Sn_6 crystals were doped with Ga at the Sn sites, contributing to this stabilization. At lower doping levels (5%), the helical phase extends slightly to higher temperatures, increasing from 370 K in the parent compound to 417 K. However, as the doping concentration reaches 22%, intraplanar AFM correlations are suppressed, resulting in a transition from paramagnetic (PM) to FM behavior below 370 K. Our research focuses on this FM phase.

In this Letter, we present an in-depth investigation into the transport, magneto-transport and the electronic structure of the kagome magnet $\text{ScMn}_6(\text{Sn}_{0.78}\text{Ga}_{0.22})_6$ in its FM state. Our methodology combines angle-resolved photoemission spectroscopy (ARPES) with density functional theory (DFT) calculations. A clear transition from paramagnetic to FM behav-

ior is observed around $T_c = 375 \text{ K}$ in $\text{ScMn}_6(\text{Sn}_{0.78}\text{Ga}_{0.22})_6$. This system exhibits strong magnetic anisotropy, favoring an in-plane easy axis. The Hall resistivity indicates substantial contribution from the anomalous Hall effect. Additionally, we identified a Dirac cone at the \bar{K} point with a binding energy of approximately 0.1 eV below the Fermi level (E_F). We also observed a flat band extending across a significant portion of the BZ, originating from the destructive interference of the wave function within the Mn kagome lattice. Theoretical calculations reveal the Dirac cone gap can be tuned by changing the magnetic moment orientation where an out-of-plane alignment creates a $\sim 15 \text{ meV}$ gap, while an in-plane orientation results in a gapless state, as confirmed by ARPES. Although strong correlations, non-trivial band topology, magnetic ordering, and geometric frustration have each been extensively studied individually, it is rare for a material family to exhibit multiple, if not all, of these characteristics simultaneously. Our study sheds light on the multifaceted nature of this material, opening new avenues for exploring its novel properties.

High-quality single crystals of $\text{ScMn}_6(\text{Sn}_{0.78}\text{Ga}_{0.22})_6$ were synthesized by the self-flux method. Magnetization measurements were carried out using the vibrating sample magnetometer (VSM). Resistivity and Hall measurements were performed using the conventional four-probe method. Synchrotron based ARPES measurements were performed at the Advanced Light Source (ALS) beamline 4.0.3 equipped with R8000 hemispherical analyzer. We performed density functional theory (DFT) based ab initio calculations using the Vienna Ab Initio Simulation Package (VASP) with Projector Augmented Wave (PAW) pseudopotentials and a plane-wave basis set [42, 43]. Details on the experimental and computational methods have been provided in the Supplemental Material (SM) section 1 [44].

$\text{ScMn}_6(\text{Sn}_{0.78}\text{Ga}_{0.22})_6$ crystallizes in the hexagonal MgFe_6Ge_6 -type structure with space-group $P6/mmm$ (No. 191), as shown in Fig. 1(a-b). Within a unit cell, two pristine Mn kagome layers exhibit a simple A-A stacking pattern, while the hexagonal structure is formed by Sn and Ga atoms, with Sc atoms positioned at the center of the hexagon. The magnetic configuration features FM Mn planes, and the kagome lattice formed by Mn atoms is illustrated in Fig. 1(b). Rietveld refinement of room temperature powder X-ray diffraction (PXRD) data using Fullprof software yielded lattice parameters of $a = b = 5.409 \text{ \AA}$ and $c = 8.846 \text{ \AA}$ (see Supplemental Material (SM) section 2 and Fig. S1) [44]. Figure 1(c) shows the bulk 3D BZ with high-symmetry points and the projected 2D BZ along the c -axis. Experimental lattice constants were used for the present DFT calculations, with the SOC calculated FM bulk band structure along the Γ -K-M direction shown in Fig. 1(d) and Fig. 1(e), with spin-quantization directions along the out-of-plane and in-plane orientations, respectively. The Dirac cone at the K-point is evident in both figures. Notably, when the spin-quantization direction is oriented out-of-plane, a small but finite gap opens in the Dirac cone, which becomes gapless when the spin-quantization direction lies in-plane.

To gain a deeper understanding of how the Dirac cone gap

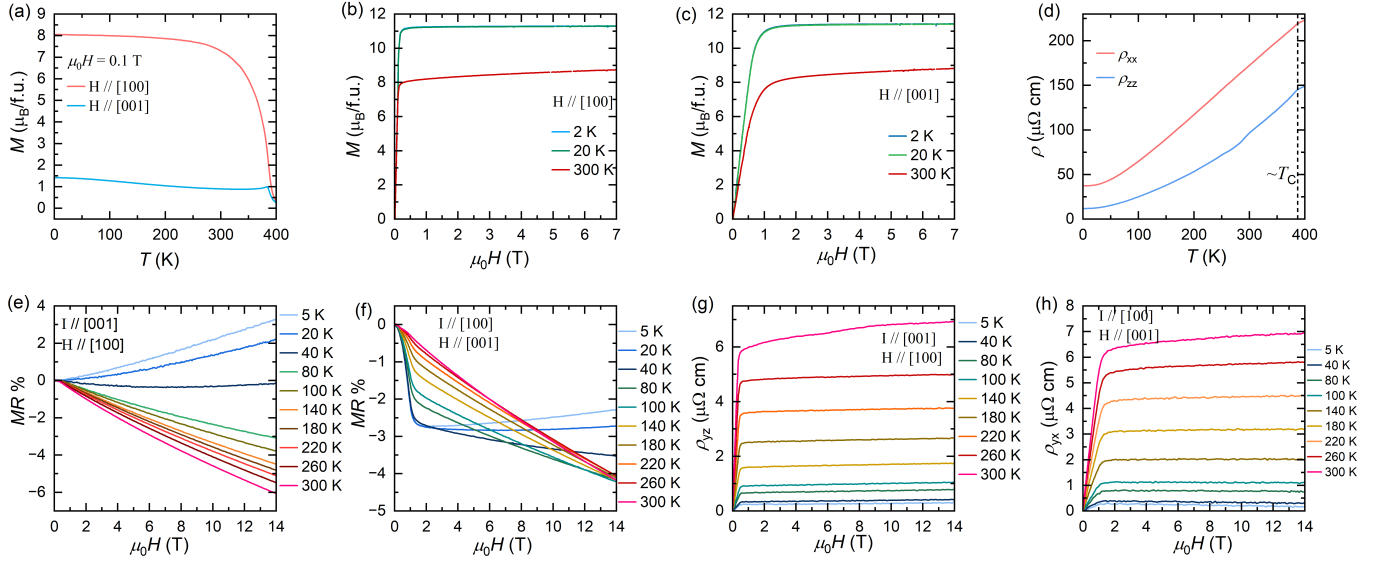


Fig. 2. Observation of in-plane ferromagnetization and the anomalous Hall effect. (a) Temperature dependence of magnetization with an applied magnetic field along the ab plane and the c -axis. (b) Isothermal magnetization curves along the ab plane and the (c) c -axis as a function of temperature. (d) Temperature dependence of the longitudinal resistivity along the ab plane and the c -axis. (e) Magnetoresistance for current along the c -axis, H is applied in the ab plane. (f) Magnetoresistance for current along the ab -plane, H is applied in the c -axis. (g) Hall resistivity along the ab -plane, I is applied along the c -axis. (h) Hall resistivity along the c -axis, I is applied along the ab -plane.

varies with the orientation of the magnetization axis, we employ a tight-binding model for the kagome lattice that incorporates a Kane-Mele SOC term. We observe that the Dirac gap size decreases as the magnetic moment rotates away from the z -axis (see Fig. S2 in the SM [44]). This gap reduction is attributed to the weakened influence of the Kane-Mele SOC as the magnetic moment aligns in the in-plane direction. To illustrate this, consider the following model for spin-polarized electrons in real space [18]:

$$H(\vec{k}) = t \sum_{\langle i,j \rangle} c_i^\dagger c_j + i\lambda \sum_{\langle i,j \rangle} \vec{S} \cdot (\vec{E}_{ij} \times \vec{R}_{ij}) c_i^\dagger c_j + \text{h.c.} \quad (1)$$

The second term represents the Kane-Mele SOC. Here, \vec{R}_{ij} is the distance vector between sites i and j , and \vec{E}_{ij} denotes the electric field experienced by electrons along \vec{R}_{ij} . Assuming the magnetization axis forms an angle θ with respect to the \hat{z} axis, the last term can be expressed as:

$$H_{\text{KM}} = i\lambda S \cos \theta \sum_{\langle i,j \rangle} \hat{z} \cdot (\vec{E}_{ij} \times \vec{R}_{ij}) c_i^\dagger c_j + \text{h.c.} \quad (2)$$

According to this expression, the strength of the Kane-Mele term reaches its maximum when the magnetization axis aligns along the z -direction, and approaches zero as the magnetization axis rotates toward the xy plane. This results in a reduced band gap in the FM- x phase compared to the FM- z phase. We note that, in real materials, the SOC may be more complex than the simplified Kane-Mele model used here. Nonetheless, this model provides an intuitive understanding of the band gap dependence at the Dirac point with respect to magnetic orientations.

Figure 2(a) shows the temperature-dependent magnetization curves along the ab plane and the c -axis at $\mu_0 H = 0.1$ T, indicating a transition from PM to FM behavior around $T_c = 375$ K in $\text{ScMn}_6(\text{Sn}_{0.78}\text{Ga}_{0.22})_6$. This system exhibits strong magnetic anisotropy, favoring an in-plane easy axis. Notably, the in-plane magnetization (red curve) surpasses the out-of-plane susceptibility (blue curve) by approximately fivefold, as shown in Fig. 2(a). Figures 2(b) and 2(c) present isothermal magnetization curves for magnetic fields parallel to the ab plane and the c -axis at various temperatures. At 2 K, the magnetizations along the ab plane and the c -axis reach saturation around 0.05 T and 1 T, respectively. Although both directions achieve a similar saturated magnetization ($\approx 11 \mu_B/\text{f.u.}$), saturation occurs more quickly along the ab plane, confirming it as the preferred direction for magnetization.

The temperature dependence of the longitudinal resistivity, with current flowing along the ab plane (ρ_{xx}) and the c -axis (ρ_{zz}), exhibits typical metallic behavior as temperature decreases from 400 K to 1.8 K. Both resistivity curves show a slight kink at 385 K, suggesting reduced charge-carrier scattering near the PM-FM ordering temperature. The magnetoresistance (MR) for $\mu_0 H = 0 - 14$ T with $I \parallel [001]$, $\mu_0 H \parallel [100]$ and $I \parallel [100]$, $\mu_0 H \parallel [001]$, is shown in Fig. 2(e) and Fig. 2(f) at selected temperatures. MR was calculated from resistivity data using the formula $\text{MR} = (\rho_{xx}(\mu_0 H) - \rho_{xx}) / \rho_{xx} \times 100\%$, where ρ_{xx} and $\rho_{xx}(\mu_0 H)$ represent zero-field and in-field resistivities, respectively. When I is along the c -axis and $\mu_0 H$ is along the a -axis [Fig. 2(e)], the MR exhibits nonlinearity across all measured temperatures. For $T \geq 40$ K, MR is negative, indicating reduced scattering due to spin disorder in the FM state at higher temperatures. However, for $T \leq 20$ K, MR becomes positive, suggesting the presence of a different

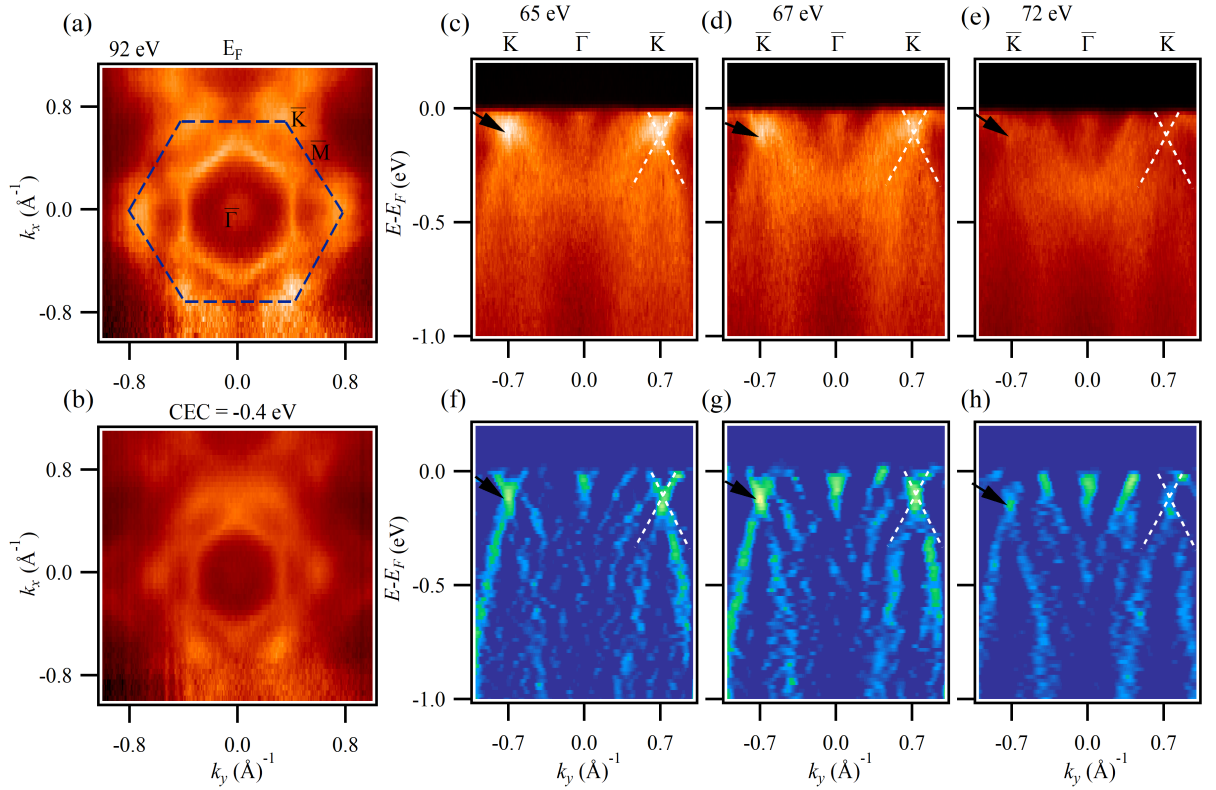


Fig. 3. Observation of Dirac cone at the \bar{K} point of the Brillouin zone. (a) ARPES measured Fermi surface (FS) measured along the (001) direction using a photon energy of 92 eV and linear horizontal (LH) polarization. High-symmetry points are labeled in black color. (b) Constant energy contour at a binding energy of - 400 meV. ARPES measured band dispersion along the \bar{K} - $\bar{\Gamma}$ - \bar{K} high symmetry line at a photon energy of (c) 65 eV, (d) 67 eV, and (e) 72 eV, respectively. (f-h) Second derivative plot of the ARPES-measured band dispersion corresponding to panels (c-e), respectively. ARPES measurements were performed at the ALS beamline 4.0.3 at a temperature of 11 K i.e., in the FM phase using LH polarization.

mechanism at low temperatures. The non-negative MR could be due to the compensation effect between two types of charge carriers [33]. Conversely, MR for $I \parallel [100]$, $\mu_0 H \parallel [001]$ remains negative across all temperatures [Fig. 2(f)]. Notably, the slope of the MR curves steepens at lower fields as the temperature decreases. To investigate the anomalous Hall effect, the Hall resistivity was measured from 5-300 K. Figures 2(g) and 2(h) show the Hall resistivities measured in two different crystallographic directions. In Fig. 2(g), ρ_{yz} represents $I \parallel [001]$, $\mu_0 H \parallel [100]$, while in Fig. 2(h), ρ_{yx} is for $I \parallel [100]$, $\mu_0 H \parallel [001]$. The Hall resistivity behavior closely resembles the magnetization data $M(H)$ shown in Fig. 2(b) and Fig. 2(c), indicating a substantial contribution from the anomalous Hall effect (AHE).

Next, to investigate the electronic structure of $\text{ScMn}_6(\text{Sn}_{0.78}\text{Ga}_{0.22})_6$, we performed high-resolution ARPES measurements on the cleaved (001) plane. The results of these measurements are shown in Figures 3-4. Figures 3(a-b) present the Fermi surface (FS) and the constant energy contour (CECs) measured with a photon energy of 92 eV and LH polarized light at a temperature of 11 K, within the FM phase; see SM section 3 and Fig. S3 for additional FS data [44]. The FS maps reveal multiple pockets at the Fermi level (E_F), consistent with the metallic character of the

material. In line with the crystal symmetry, the FS displays hexagonal symmetry. Notably, the FS includes a small circular pocket at the $\bar{\Gamma}$ high-symmetry point, while along the $\bar{\Gamma}$ - \bar{M}/\bar{K} high-symmetry line, a hexagonal pocket emerges. These pockets gradually diminish with increasing binding energy, indicating their electron-like nature. Additionally, intense circular features appear at the BZ corners, corresponding to the \bar{K} points. The DFT-calculated bulk FS and CEC are shown in Fig. S4; see SM Section 3 for details [44], demonstrating a reasonable match to the observed ARPES spectra.

Subsequently, we analyzed the band dispersion along various high-symmetry directions as shown in Figs. 3(c-h) and 4. Figure 3(c) illustrates the ARPES-measured band-dispersion along the \bar{K} - $\bar{\Gamma}$ - \bar{K} high-symmetry line, captured using a photon energy of 65 eV. A small electron-like pocket is visible at the $\bar{\Gamma}$ point, while the spectra reveal a Dirac cone at the \bar{K} point, with the Dirac point located at approximately $E-E_F \approx -0.1$ eV, as indicated by the white dashed lines for clarity. Measurements conducted with photon energies of 67 eV and 72 eV, shown in Figs. 3(d-e), demonstrate that while the intensity of the band forming the Dirac cone vary, the band remain distinctly visible. The Dirac cone at the \bar{K} point is more clearly visualized in the second-derivative plots in Figs.

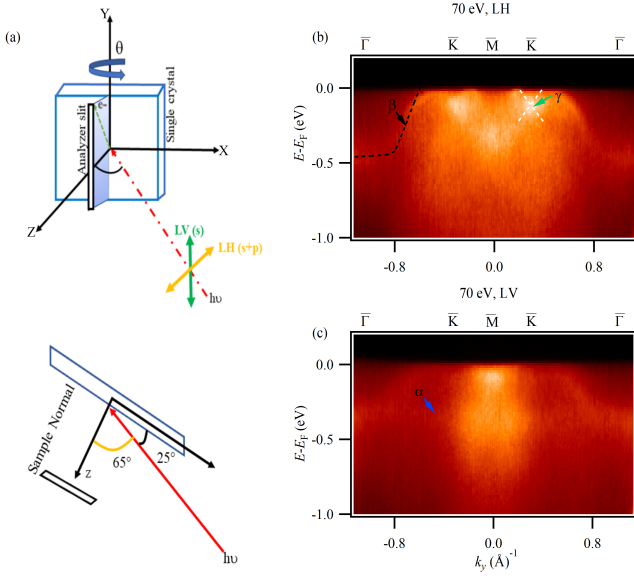


Fig. 4. Polarization-dependent behavior of the flat band and Dirac cone. (a) Experimental geometry used for polarization-dependent ARPES measurements. Experimental band dispersion measured along the $\bar{\Gamma}$ - \bar{K} - \bar{M} - \bar{K} - $\bar{\Gamma}$ high-symmetry line using (b) LH polarization and (c) LV polarization. The symbols α , β , and γ represent the flat band, parabolic band, and Dirac cone, respectively. ARPES measurements were performed at the ALS beamline 4.0.3 at a temperature of 11 K i.e., in the FM phase using both LH and LV polarization.

3(f-h), where it is highlighted by white-dashed lines and black arrows for clarity. The DFT-calculated band dispersion along the \bar{K} - $\bar{\Gamma}$ - \bar{K} line, presented in Fig. S5, clearly shows the Dirac cone (see SM section 4 for further details [44]). Its appearance in bulk DFT calculations indicates a bulk origin for the Dirac cone.

To gain further insights into the orbital character of the electronic bands, we conducted polarization-dependent ARPES measurements. Figure 4(a) shows the experimental setup, where measurements were performed along the $\bar{\Gamma}$ - \bar{K} - \bar{M} - \bar{K} - $\bar{\Gamma}$ high-symmetry line using linear horizontal (LH) and linear vertical (LV) polarizations, as depicted in Fig. 4(b-c), respectively. As evident from the figure, different sets of bands are selectively enhanced under LH and LV polarized light, respectively, revealing interesting distinctions between the two data sets. A flat band denoted as α at approximately ~ -0.4 eV binding energy is detected with LV polarization but not with LH, suggesting these features arise from different orbitals. A dispersive band, labeled β , crosses the E_F and extends from the \bar{K} to the $\bar{\Gamma}$ high-symmetry line. Although this band is slightly more intense with LH polarization, it remains visible in both LH and LV polarizations. Notably, a Dirac cone appears at the \bar{K} point under LH polarization but is absent under LV polarization (see SM section 4-5 and Fig. S6-S7 for additional photon energy dependent ARPES measurements along the $\bar{\Gamma}$ - \bar{K} - \bar{M} - \bar{K} - $\bar{\Gamma}$ line [44]). Following the selection rules in photoemission, the ability to selectively excite bands depends on their orbital symmetry relative to specific mirror planes within the setup. Specifically, polarizations with the

electric field vector aligned either parallel or perpendicular to the mirror plane distinguish orbitals with even or odd parity concerning the mirror plane. When aligning the $\bar{\Gamma}$ - \bar{K} - \bar{M} - \bar{K} - $\bar{\Gamma}$ high-symmetry line along the analyzer slit (i.e., along the y - z mirror plane), LV polarization suppresses odd orbitals and detects even orbitals. Based on selection rules, the α band is attributed to Mn $d_{x^2-y^2}$, d_{z^2} , and d_{yz} orbitals. Using similar arguments, the γ band originates from Mn d_{xy} and Mn d_{xz} orbitals.

While no ARPES studies have been reported on the parent material ScMn_6Sn_6 or $\text{ScMn}_6(\text{Sn}_{0.78}\text{Ga}_{0.22})_6$, some Mn-based kagome materials have been investigated using ARPES. Magnetic measurements on YMn_6Sn_6 reveal two transition temperatures: $T_N = 359$ K, corresponding to a paramagnetic-to-AFM transition, and $T_{hel} = 326$ K, where a c -axis helical order with in-plane ferromagnetism emerges [29]. ARPES studies on YMn_6Sn_6 have shown that it hosts a Dirac cone, with the Dirac point located 45 meV below the E_F in the AFM phase [29]. In contrast, TbMn_6Sn_6 exhibits a ferrimagnetic ground state with a Curie temperature of 423 K [6]. Magnetization measurements on TbMn_6Sn_6 show a well-defined hysteresis loop when the field is applied along the c -axis but no loop when applied in the a - b plane, confirming strong out-of-plane magnetization. Notably, scanning tunnelling microscopy and ARPES measurements on TbMn_6Sn_6 reveal a large Chern gap at 130 meV above E_F in the ferrimagnetic ground state [6]. Another material, ErMn_6Sn_6 undergoes a paramagnetic-to-AFM transition at $T_N = 345$ K, followed by a ferrimagnetic transition below 68 K [30]. However, ARPES measurements did not reveal clear Dirac cones or flat bands in its ferrimagnetic ground state [30]. Similarly, HoMn_6Sn_6 transitions from a paramagnetic to a ferrimagnetic state below 376 K and undergoes a spin-reorientation transition below 200 K [31]. ARPES studies on HoMn_6Sn_6 suggest that the Dirac cone lie above E_F , while flat bands remain undetected [31]. In comparison, $\text{ScMn}_6(\text{Sn}_{0.78}\text{Ga}_{0.22})_6$ adopts a FM ground state at low temperatures without undergoing additional magnetic transitions, making it an excellent system for studying metallic behavior without the complexities of multiple magnetic phases. The Dirac point in $\text{ScMn}_6(\text{Sn}_{0.78}\text{Ga}_{0.22})_6$ is located approximately 100 meV below E_F , slightly lower than in YMn_6Sn_6 (45 meV below E_F) [29], while in TbMn_6Sn_6 , the Dirac point is positioned 130 meV above E_F [6]. The magnetic behavior of $\text{ScMn}_6(\text{Sn}_{0.78}\text{Ga}_{0.22})_6$ contrasts with that of its parent compound, ScMn_6Sn_6 , which undergoes AFM ordering below $T_N = 390$ K and transitions through multiple magnetic phases under an external magnetic field [41]. A key result of this study is the successful doping of 22 % Ga at Sn sites in ScMn_6Sn_6 , stabilizing ferromagnetism with an in-plane easy axis in $\text{ScMn}_6(\text{Sn}_{0.78}\text{Ga}_{0.22})_6$. The material undergoes a paramagnetic-to-FM transition at $T_c = 375$ K, distinguishing it from the above discussed Mn-based 166 kagome metals. Notably, the in-plane magnetization of $\text{ScMn}_6(\text{Sn}_{0.78}\text{Ga}_{0.22})_6$ is approximately five times greater than its out-of-plane susceptibility, further highlighting its unique magnetic anisotropy.

In summary, we have tuned the magnetic properties of ScMn_6Sn_6 by incorporating Ga as dopant, yielding the com-

pound $\text{ScMn}_6(\text{Sn}_{0.78}\text{Ga}_{0.22})_6$, which exhibits FM behavior below 375 K, with an in-plane easy magnetization axis. Hall resistivity measurements reveal a prominent anomalous Hall effect, accompanied by the observation of a Dirac cone near E_F in both ARPES experiments and DFT calculations. Additionally, we identify flat bands extending to a significant section of the BZ, originating from the destructive interference within the Mn kagome lattice. In a broader perspective, our research offers new pathways for investigating the diverse and intriguing physics of these Mn-based kagome lattices.

M.N. acknowledges support from the Air Force Office of Scientific Research MURI (Grant No. FA9550-20-1-0322) and the US Department of Energy (DOE), Office of Science, Basic Energy Sciences grant number DE-SC0024304. DGM acknowledges the support from AFOSR MURI (Novel Light-Matter Interactions in Topologically Non-Trivial Weyl Semimetal Structures and Systems), grant FA9550-20-1-0322. The work at Northeastern University was supported by the Air Force Office of Scientific Research under Award No. FA9550-20-1-0322, and it benefited from the computational resources of Northeastern University's Advanced Scientific Computation Center (ASCC) and the Discovery Cluster. This research used resources of the Advanced Light Source, a U.S. Department of Energy Office of Science User Facility, under Contract No. DE-AC02-05CH11231. We thank Jonathan Denlinger for beamline assistance at the Advanced Light Source (ALS), Lawrence Berkeley National Laboratory.

References

- [1] T.-H. Han, J. S. Helton, S. Chu, D. G. Nocera, J. A. Rodriguez-Rivera, C. Broholm, and Y. S. Lee, *Nature* **492**, 406 (2012).
- [2] H.-M. Guo and M. Franz, *Phys. Rev. B* **80**, 113102 (2009).
- [3] L. Ye, M. Kang, J. Liu, F. Von Cube, C. R. Wicker, T. Suzuki, C. Jozwiak, A. Bostwick, E. Rotenberg, and D. C. Bell, *Nature* **555**, 638 (2018).
- [4] Z. Lin, J.-H. Choi, Q. Zhang, W. Qin, S. Yi, P. Wang, L. Li, Y. Wang, H. Zhang, and Z. Sun, *Phys. Rev. Lett.* **121**, 096401 (2018).
- [5] J.-X. Yin, S. S. Zhang, G. Chang, Q. Wang, S. S. Tsirkin, Z. Guguchia, B. Lian, H. Zhou, K. Jiang, and I. Belopolski, *Nat. Phys.* **15**, 443 (2019).
- [6] J.-X. Yin, W. Ma, T. A. Cochran, X. Xu, S. S. Zhang, H.-J. Tien, N. Shumiya, G. Cheng, K. Jiang, B. Lian, Z. Song, G. Chang, I. Belopolski, D. Multer, M. Litskevich, Z.-J. Cheng, X. P. Yang, B. Swidler, H. Zhou, H. Lin, T. Neupert, Z. Wang, N. Yao, T.-R. Chang, S. Jia, and M. Zahid Hasan, *Nature* **583**, 533 (2020).
- [7] N. J. Ghimire and I. I. Mazin, *Nat. Mater.* **19**, 137 (2020).
- [8] M. Kang, L. Ye, S. Fang, J.-S. You, A. Levitan, M. Han, J. I. Facio, C. Jozwiak, A. Bostwick, E. Rotenberg, M. K. Chan, R. D. McDonald, D. Graf, K. Kaznatcheev, E. Vescovo, D. C. Bell, E. Kaxiras, J. van den Brink, M. Richter, M. Prasad Ghimire, J. G. Checkelsky, and R. Comin, *Nat. Mater.* **19**, 163 (2020).
- [9] M. Kang, S. Fang, L. Ye, H. C. Po, J. Denlinger, C. Jozwiak, A. Bostwick, E. Rotenberg, E. Kaxiras, J. G. Checkelsky, and R. Comin, *Nat. Commun.* **11**, 4004 (2020).
- [10] M. Li, Q. Wang, G. Wang, Z. Yuan, W. Song, R. Lou, Z. Liu, Y. Huang, Z. Liu, H. Lei, Z. Yin, and S. Wang, *Nat. Commun.* **12**, 3129 (2021).
- [11] S. Regmi, T. Fernando, Y. Zhao, A. P. Sakhya, G. Dhakal, I. Bin Elius, H. Vazquez, J. D. Denlinger, J. Yang, J.-H. Chu, X. Xu, T. Cao, and M. Neupane, *Commun Mater* **3**, 100 (2022).
- [12] S. Regmi, A. P. Sakhya, T. Fernando, Y. Zhao, D. Jeff, M. Sprague, F. Gonzalez, I. Bin Elius, M. I. Mondal, and N. Valadez, D. Jarrett, A. Agosto, J. Yang, J.-H. Chu, S. I. Khondaker, X. Xu, T. Cao, M. Neupane, *Phys. Rev. B* **108**, L121404 (2023).
- [13] Z. J. Cheng, I. Belopolski, H. J. Tien, T. A. Cochran, X. P. Yang, W. Ma, J. X. Yin, D. Chen, J. Zhang, and C. Jozwiak, *Adv. Mater.* **35**, 2205927 (2023).
- [14] A. P. Sakhya, B. R. Ortiz, B. Ghosh, M. Sprague, M. I. Mondal, M. Matzelle, I. Bin Elius, N. Valadez, D. G. Mandrus, and A. Bansil, *Commun Mater* **5**, 241 (2024).
- [15] A. P. Sakhya, B. R. Ortiz, B. Ghosh, M. Sprague, M. I. Mondal, M. Matzelle, N. Atlam, A. K. Kumay, D. G. Mandrus, and J. D. Denlinger, *arXiv:2503.15759* (2025).
- [16] P. Park, B. R. Ortiz, M. Sprague, A. P. Sakhya, S. A. Chen, M. Frontzek, W. Tian, R. Sibille, D. G. Mazzone, and C. Tabata, *Nat Commun* **16**, 4384 (2025).
- [17] M. I. Mondal, A. P. Sakhya, M. Sprague, B. R. Ortiz, M. Matzelle, B. Ghosh, N. Valadez, I. B. Elius, A. Bansil, and M. Neupane, *arXiv:2311.11488* (2023).
- [18] E. Tang, J.-W. Mei, and X.-G. Wen, *Phys. Rev. Lett.* **106**, 236802 (2011).
- [19] G. Xu, B. Lian, and S.-C. Zhang, *Phys. Rev. Lett.* **115**, 186802 (2015).
- [20] D. Xiao, M.-C. Chang, and Q. Niu, *Rev. Mod. Phys.* **82**, 1959 (2010).
- [21] S. Nakatsuji, N. Kiyohara, and T. Higo, *Nature* **527**, 212 (2015).
- [22] A. K. Nayak, J. E. Fischer, Y. Sun, B. Yan, J. Karel, A. C. Komarek, C. Shekhar, N. Kumar, W. Schnelle, J. Kübler, C. Felser, and S. S. P. Parkin, *Sci. Adv.* **2**, e1501870 (2016).
- [23] E. Liu, Y. Sun, N. Kumar, L. Muechler, A. Sun, L. Jiao, S.-Y. Yang, D. Liu, A. Liang, Q. Xu, J. Kroder, V. Süß, H. Borrmann, C. Shekhar, Z. Wang, C. Xi, W. Wang, W. Schnelle, S. Wirth, Y. Chen, S. T. B. Goennenwein, and C. Felser, *Nat. Phys.* **14**, 1125 (2018).
- [24] W. Ma, X. Xu, J.-X. Yin, H. Yang, H. Zhou, Z.-J. Cheng, Y. Huang, Z. Qu, F. Wang, M. Z. Hasan, and S. Jia, *Phys. Rev. Lett.* **126**, 246602 (2021).
- [25] R. S. Li, T. Zhang, W. Ma, S. X. Xu, Q. Wu, L. Yue, S. J. Zhang, Q. M. Liu, Z. X. Wang, T. C. Hu, X. Y. Zhou, D. Wu, T. Dong, S. Jia, H. Weng, and N. L. Wang, *Phys. Rev. B* **107**, 045115 (2023).
- [26] X. Gu, C. Chen, W. S. Wei, L. L. Gao, J. Y. Liu, X. Du, D. Pei, J. S. Zhou, R. Z. Xu, Z. X. Yin, W. X. Zhao, Y. D. Li, C. Jozwiak, A. Bostwick, E. Rotenberg, D. Backes, L. S. I. Veiga, S. Dhesi, T. Hesjedal, G. van der Laan, H. F. Du, W. J. Jiang, Y. P. Qi, G. Li, W. J. Shi, Z. K. Liu, Y. L. Chen, and L. X. Yang, *Phys. Rev. B* **105**, 155108 (2022).
- [27] T. Asaba, S. M. Thomas, M. Curtis, J. D. Thompson, E. D. Bauer, and F. Ronning, *Phys. Rev. B* **101**, 174415 (2020).
- [28] H. Zeng, G. Yu, X. Luo, C. Chen, C. Fang, S. Ma, Z. Mo, J. Shen, M. Yuan, and Z. Zhong, *J. Alloys Compd.* **899**, 163356 (2022).
- [29] N. J. Ghimire, R. L. Dally, L. Poudel, D. C. Jones, D. Michel, N. T. Magar, M. Bleuel, M. A. McGuire, J. S. Jiang, J. F. Mitchell, J. W. Lynn, and I. I. Mazin, *Sci. Adv.* **6**, eabe2680 (2020).
- [30] G. Dhakal, F. Cheenicode Kabeer, A. K. Pathak, F. Kabir, N. Poudel, R. Filippone, J. Casey, A. P. Sakhya, S. Regmi, C. Sims, K. Dimitri, P. Manfrinetti, K. Gofryk, P. M. Oppeneer, and M. Neupane, *Phys. Rev. B* **104**, L161115 (2021).
- [31] F. Kabir, R. Filippone, G. Dhakal, Y. Lee, N. Poudel, J. Casey, A. P. Sakhya, S. Regmi, R. Smith, P. Manfrinetti, L. Ke, K. Gofryk, M. Neupane, and A. K. Pathak, *Phys. Rev. Mater.* **6**, 064404 (2022).

- [32] B. Lv, R. Zhong, X. Luo, S. Ma, C. Chen, S. Wang, Q. Luo, F. Gao, C. Fang, W. Ren, and Z. Zhong, *J. Alloys Compd.* **957**, 170356 (2023).
- [33] D. Chen, C. Le, C. Fu, H. Lin, W. Schnelle, Y. Sun, and C. Felser, *Phys. Rev. B* **103**, 144410 (2021).
- [34] L. Gao, S. Shen, Q. Wang, W. Shi, Y. Zhao, C. Li, W. Cao, C. Pei, J.-Y. Ge, G. Li, J. Li, Y. Chen, S. Yan, and Y. Qi, *Appl. Phys. Lett.* **119**, (2021).
- [35] W. Ma, X. Xu, Z. Wang, H. Zhou, M. Marshall, Z. Qu, W. Xie, and S. Jia, *Phys. Rev. B* **103**, 235109 (2021).
- [36] Q. Wang, K. J. Neubauer, C. Duan, Q. Yin, S. Fujitsu, H. Hosono, F. Ye, R. Zhang, S. Chi, K. Krycka, H. Lei, and P. Dai, *Phys. Rev. B* **103**, 014416 (2021).
- [37] N.J. Ghimire, R.L. Dally, L. Poudel, D.C. Jones, D. Michel, N.T. Magar, M. Bleuel, M.A. McGuire, J.S. Jiang, and I.I. Mazin, *Sci. Adv.* **6** 2680 (2022).
- [38] B. Malaman, G. Venturini, and B. Roques, *Mater. Res. Bull.* **23**, 1629 (1988).
- [39] G. Venturini, B. C. El Idrissi, and B. Malaman, *J. Magn. Magn. Mater.* **94**, 35 (1991).
- [40] H. Zhang, C. Liu, Y. Zhang, Z. Hou, X. Fu, X. Zhang, X. Gao, and J. Liu, *Appl. Phys. Lett.* **121**, 202401 (2022).
- [41] R. P. Madhugaria, S. Mozaffari, H. Zhang, W. R. Meier, S.-H. Do, R. Xue, T. Matsuoka, and D. G. Mandrus, *Phys. Rev. B* **108**, 125114 (2023).
- [42] G. Kresse and J. Furthmüller, *Phys. Rev. B* **54**, 11169 (1996).
- [43] G. Kresse and D. Joubert, *Phys. Rev. B* **59**, 1758 (1999).
- [44] See Supplemental Material for experimental and computational details, sample characterization, photon-energy dependent measurements, and additional experimental and DFT analyses. It also includes Refs. [45-48].
- [45] P. C. Canfield, T. Kong, U. S. Kaluarachchi, and N. H. Jo, *Philos. Mag.* **96**, 84 (2016).
- [46] J. P. Perdew, K. Burke, and M. Ernzerhof, *Phys. Rev. Lett.* **77**, 3865 (1996).
- [47] G. Pizzi, V. Vitale, R. Arita, S. Blügel, F. Freimuth, G. Géranton, M. Gibertini, D. Gresch, C. Johnson, T. Koretsune, J. Ibañez-Azpiroz, H. Lee, J.-M. Lihm, D. Marchand, A. Marrazzo, Y. Mokrousov, J. I. Mustafa, Y. Nohara, Y. Nomura, L. Paulatto, S. Poncé, T. Ponweiser, J. Qiao, F. Thöle, S. S. Tsirkin, M. Wierzbowska, N. Marzari, D. Vanderbilt, I. Souza, A. A. Mostofi, and J. R. Yates, *J. Phys. Condens. Matter.* **32**, 165902 (2020).
- [48] J. Rodríguez-Carvajal, *Phys. B: Condens. Matter* **192**, 55 (1993).